J. Fluid Mech. (2004), *vol.* 521, *pp.* 353–379.
DOI: 10.1017/S0022112004001193 Printed in the United Kingdom

Uniaxial extensional flows in liquid bridges

By EBERHARD BÄNSCH[1], CHRISTIAN P. BERG[2] AND ANTJE OHLHOFF[2]

[1]Weierstrass Institute for Applied Analysis and Stochastics, Mohrenstrasse 39, D-10117 Berlin, and Freie Universität Berlin, Arnimallee 2–6, D-14195 Berlin, Germany

[2]Center of Applied Space Technology and Microgravity (ZARM), University of Bremen, Am Fallturm, Bremen, D-28359, Germany

(Received 3 August 2003 and in revised form 1 July 2004)

In this paper we consider the possibility of generating homogeneous flows with a nearly constant strain rate. This is achieved by stretching an almost cylindrical liquid bridge under microgravity. One key issue is the adjustability of the disk diameters, necessary for maintaining ideal boundary conditions. We first study the stretching of two different fluids by both numerical and experimental means. The numerical results are compared with the experimental data and very good agreement is found. The numerical method is then used to study the behaviour of liquid bridges for quite a large range of the flow parameters (capillary number *Ca* and Weber number *We*) in order to detect those regimes with most suitable flow conditions.

1. Introduction

Linear flow fields are commonly used for rheological studies, e.g. to measure the fluid viscosity or the deformation behaviour of the whole sample or components in it. The fluid properties may vary considerably depending on the specific linear flow type and the corresponding homogeneity of the flow field. In view of the experimental demands of rheological tests, the ideal uniaxial extensional flow field is characterized by a constant strain rate distribution, both in space and time.

The ideal uniaxial extensional flow field $\boldsymbol{v}$ with constant strain rate $\dot{\epsilon}_0$ in space and time has the form

$$v_r = -0.5\dot{\epsilon}_0 r, \quad v_\theta = 0, \quad v_z = \dot{\epsilon}_0 z, \tag{1.1}$$

in a cylindrical coordinate system (r, θ, z). For an initially cylindrical fluid volume with length L_0 and radius R_0 this specific form of $\boldsymbol{v}$ implies

$$L(t) = L_0 \exp(\dot{\epsilon}_0 t), \tag{1.2}$$

$$R(t) = R_0 \exp(-0.5\,\dot{\epsilon}_0 t), \tag{1.3}$$

with $L(t)$ the time-dependent length of the fluid volume and $R(t)$ its radius. In particular, the liquid bridge is cylindrical in shape at all times.

However, the experimental realization of such a flow field causes severe difficulties in practice. Several attempts have been made in this direction. For instance Chin & Han (1979) and Mighri, Ajji & Carreau (1997) used a conical section of a transparent flow channel to investigate the deformation of emulsion droplets. Although this device is capable of providing an extensional flow within the entrance length of the conical channel, this extensional flow is predominantly non-constant and heterogeneous owing to the developing velocity profile in the entrance region of the conical channel.

Because of the difficulties in generating homogeneous shear-free uniaxial extensional flows in convergent channels, plane extensional flows were principally generated when performing droplet deformation experiments, see Stone (1994). A guidance to generate ideal plane extensional flow within a four-roll mill is given by Higdon (1993).

However, plane extensional flows are not optimal for the investigation of embedded axially symmetric emulsion droplets or particles owing to the breaking of the two-dimensional character of the flow, see also Berg (2002). For a comparison of say, droplet experiments with theoretical results, uniaxial extensional flows are more adequate.

Even for stretched liquid bridges, care must be taken to achieve a flow field with high quality, which depends on the actual inertia, capillary and viscous forces and appropriate boundary conditions. For instance, Kröger *et al.* (1992) have shown that the contour deformation of an initially cylindrical liquid bridge between two unchanging endplates during stretching yields large variations of the local extension rates in space and time caused by necking.

To circumvent this effect and to obtain a constant extension rate, at least in the middle of the bridge, Tirtaatmadja & Sridhar (1993) proposed adjusting the disk velocity profile; but, even this attempt leads to a flow field which remains far from homogeneous.

In this paper, we discuss the possibility of generating nearly homogeneous flows with an almost constant strain rate in a stretched fluid column by means of adjusting the disk diameters so that ideal boundary conditions for producing a cylindrical fluid bridge are maintained.

Even under microgravity conditions and with adjustment of the disk diameters, the ideal extensional flow is not totally achievable; this is due to the dynamic pressure gradient (induced by acceleration and capillary forces) deforming the bridge contour (see Berg, Dreyer & Rath 1999). Instead, the real stretched liquid bridge is asymmetrically deformed in the direction of the accelerated support owing to inertia and surface tension forces and will eventually pinch off.

Our goal is to investigate this behaviour with respect to the flow parameters Ca (capillary number) and We (Weber number), see § 2, and detect those regimes with the most suitable flow conditions.

To this end, we first study the stretching of two different liquids by both numerical and experimental means. The numerical results are compared with the experimental data, resulting in very good agreement. The numerical method is then used to study the behaviour of liquid bridges for a fairly large range of Ca and We values.

For the numerical simulation of the problem we use a finite-element method with the following key ingredients: a variational formulation for the curvature of the free boundary, yielding an accurate dimensionally-independent and simple-to-implement approximation for the curvature; a stable time discretization, semi-implicit with respect to the treatment of the curvature terms. This first allows us to choose the time step independently of the mesh size in contrast to common ‘explicit’ treatments of the curvature terms, and secondly decouples the computation of the geometry and the flow field. This approach has proved to be both efficient and robust with respect to the dimensionless parameters Ca, We, see Bänsch (2001) and also § 3.

In some related work, Meissner (1969) developed the extensional rheometer, also known as the rheotens test, which was modified by Maia *et al.* (1999). Matta & Tytus (1988) and Sridhar *et al.* (1991) pointed out the relevance of constant strain rate distributions in the full sample and developed the pioneering filament stretching device. Such stretching devices were in turn used by several research groups (e.g.

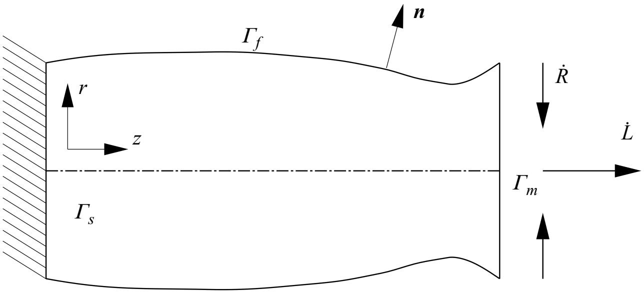

FIGURE 1. Setting and basic notation. The device is dropped in the z-direction.

Tirtaatmadja & Sridhar 1993; Berg, Kröger & Rath 1994; Spiegelberg, Ables & McKinley 1996; Yao, Spiegelberg & McKinley 2000; McKinley & Tripathi 2000; McKinley & Sridhar 2002), to measure the extensional viscosity in macromolecular fluids.

In addition to this experimental work, numerical simulations have been performed (e.g. Gaudet, McKinley & Stone 1996; Yao, Spiegelberg & McKinley 2000; Yildirim & Basaran 2001). The latter work studies the dependence of the limiting bridge length and the location of the breakup point on the constant stretching speed (and therefore non-constant strain rate). In Olagunju (1999), a linear stability analysis for a one-dimensional model neglecting inertia and gravity forces is considered.

Note that in contrast to our work, all these articles consider stretched liquid bridges with constant disk diameters. In the present work, we are capable of identifying regimes with nearly constant strain rate distribution (in both space and time) owing to the adjustability of the disk diameters.

We also remark that this study exclusively considers stretching of liquid bridges in the first time period preceding the beginning of the breakup process. Details about the special breakup process with its well-known self-similarity and scaling behaviour can be found, for example, in the review paper of Eggers (1997).

The rest of the paper is organized as follows: in § 2, we present the mathematical formulation of the problem. In § 3, a brief outline of the numerical method is given and § 4 describes the experimental set-up and experimental conditions. In § 5, we first compare the experiments with corresponding simulations and then discuss a numerical parameter study for the dimensionless parameters *Ca* and *We*. Our results are summarized in § 6.

2. Problem formulation

2.1. *Mathematical formulation*

Denote by $\Omega = \Omega(t)$ the region occupied by the liquid; Ω is dependent on the position of the membranes Γ_s, Γ_m (the solid and moving endplates, respectively) and on the *a priori* unknown free surface Γ_f (see figure 1). We consider an isothermal incompressible and Newtonian fluid with constant density ρ and dynamical viscosity μ. Therefore the system can be described by the incompressible Navier–Stokes equations: find a vector-valued velocity field $\boldsymbol{v} = \boldsymbol{v}(t, \boldsymbol{x})$ and a pressure field $p = p(t, \boldsymbol{x})$ such that

$$\rho(\partial_t \boldsymbol{v} + \boldsymbol{v} \cdot \nabla \boldsymbol{v}) - \nabla \cdot \boldsymbol{\sigma} = \rho \boldsymbol{g} \quad \text{in } \Omega, \qquad (2.1a)$$

$$\nabla \cdot \boldsymbol{v} = 0 \quad \text{in } \Omega. \qquad (2.1b)$$

Here, $\boldsymbol{g} = g\,\boldsymbol{e}_z$ denotes the vector of gravity and $\boldsymbol{\sigma} = \boldsymbol{\sigma}(\mu\,\boldsymbol{v}, p)$ denotes the stress tensor, defined by

$$\boldsymbol{\sigma} = 2\mu\,\boldsymbol{D}(v) - p\boldsymbol{I} = \mu(\nabla\boldsymbol{v} + \nabla\boldsymbol{v}^T) - p\boldsymbol{I}.$$

Note that in order to avoid confusion, vector- as well as matrix-valued functions will be denoted by bold characters, whereas plain characters indicate scalars.

On the free surface Γ_f we have a balance of forces

$$\boldsymbol{\sigma}\cdot\boldsymbol{n} = -\gamma\left(\frac{1}{R_1} + \frac{1}{R_2}\right)\boldsymbol{n} + \boldsymbol{\sigma}_{gas}\cdot\boldsymbol{n},$$

with γ the coefficient of surface tension, $1/R_1$, $1/R_2$ the principle curvatures of Γ_f, $\boldsymbol{n}$ the (outward pointing) normal vector to Γ_f and $\boldsymbol{\sigma}_{gas}$ the stress tensor of the ambient gas phase. Since the dynamic part of the latter is negligible, we obtain

$$\boldsymbol{\sigma}\cdot\boldsymbol{n} = -\gamma\left(\frac{1}{R_1} + \frac{1}{R_2}\right)\boldsymbol{n} - p_{gas}\boldsymbol{n}, \tag{2.2}$$

with p_{gas} being the constant ambient pressure. Finally, the kinematic condition

$$\boldsymbol{v}\cdot\boldsymbol{n} = V_f,$$

holds, where V_f is the normal velocity of the free surface Γ_f.

On the remaining parts Γ_s, Γ_m of the boundary, no-slip conditions for $\boldsymbol{v}$ hold.

2.2. *Non-dimensional axisymmetric equations*

The following non-dimensionalization is applied:

$$\hat{\boldsymbol{x}} = \frac{1}{R_0}\boldsymbol{x}, \quad \hat{t} = \dot{\epsilon}_0 t, \quad \hat{\boldsymbol{v}} = \frac{1}{\dot{\epsilon}_0 R_0}\boldsymbol{v}, \quad \hat{p} = \frac{R_0}{\gamma}(p - p_{gas}).$$

Introducing the Weber number *We*, the capillary number *Ca*, the Bond number *Bo*, and for convenience the Reynolds number *Re*,

$$We = \frac{\rho R_0^3 \dot{\epsilon}_0^2}{\gamma}, \quad Ca = \frac{\mu R_0 \dot{\epsilon}_0}{\gamma}, \quad Bo = \frac{\rho\, R_0^2 g}{\gamma}, \quad Re = \frac{We}{Ca},$$

equation (2.1) becomes

$$We(\partial_{\hat{t}}\hat{\boldsymbol{v}} + \hat{\boldsymbol{v}}\cdot\hat{\nabla}\hat{\boldsymbol{v}}) - Ca\,\hat{\Delta}\hat{\boldsymbol{v}} + \hat{\nabla}\hat{p} = Bo\,\boldsymbol{e}_z \quad \text{in } \hat{\Omega}, \tag{2.3a}$$

$$\hat{\nabla}\cdot\hat{\boldsymbol{v}} = 0 \quad \text{in } \hat{\Omega}, \tag{2.3b}$$

On the free surface $\hat{\Gamma}_f$ we have

$$-\hat{\boldsymbol{\sigma}}(Ca\,\hat{\boldsymbol{v}}, \hat{p})\cdot\boldsymbol{n} = \hat{\kappa}\,\boldsymbol{n}, \tag{2.3c}$$

$$\hat{\boldsymbol{v}}\cdot\boldsymbol{n} = \hat{V}_f, \tag{2.3d}$$

where $\hat{\kappa}$ is the sum of the principal curvatures of $\hat{\Gamma}_f$. In our case, $Bo = 0$ (cf. §4.2), thus the dimensionless system is characterized by the ratio of inertia and capillary forces *We*, the ratio of viscous and capillary forces *Ca*, and the initial aspect ration $\Lambda_0 = L_0/R_0$. Since we only work in non-dimensional quantities, we henceforth drop the '$\hat{\ }$' for the sake of brevity and relabel the scaled variables again by $\boldsymbol{v}$, p, etc. unless otherwise stated.

Note that the fixed and moving boundaries are given in non-dimensional coordinates by

$$\Gamma_s = \{\boldsymbol{x} \mid 0 \leqslant r \leqslant \exp(-t/2), z = 0\}, \tag{2.4}$$

$$\Gamma_m = \{\boldsymbol{x} \mid 0 \leqslant r \leqslant \exp(-t/2), z = \Lambda_0 \exp(t)\}, \tag{2.5}$$

and that in non-dimensional units the (desired) strain rate is 1.

Since all data are axisymmetric and the flow is laminar we may assume a two-dimensional axisymmetric configuration, i.e.

$$\boldsymbol{v}(t, \boldsymbol{x}) = v_r(t, r, z)\boldsymbol{e}_r + v_z(t, r, z)\boldsymbol{e}_z, \quad p(t, \boldsymbol{x}) = p(t, r, z).$$

In cylindrical coordinates, the non-dimensional problem now reads:

$$We(\partial_t v_r + \boldsymbol{v}\cdot\nabla v_r) + Ca\left(-\Delta_{r,z} v_r + \frac{v_r}{r^2}\right) + \partial_r p = 0, \tag{2.6a}$$

$$We(\partial_t v_z + \boldsymbol{v}\cdot\nabla v_z) - Ca\,\Delta_{r,z} v_z + \partial_z p = 0, \tag{2.6b}$$

$$\frac{1}{r}\partial_r(r\,v_r) + \partial_z v_z = 0, \tag{2.6c}$$

where $\Delta_{r,z}\, v = (1/r)\,\partial_r(r\partial_r v) + \partial_z^2 v$ is the Laplacian in cylindrical coordinates. On the free surface Γ_f, we have

$$-Ca\begin{bmatrix} 2\partial_r v_r & \partial_r v_z + \partial_z v_r \\ \partial_r v_z + \partial_z v_r & 2\partial_z v_z \end{bmatrix}\begin{bmatrix} n_r \\ n_z \end{bmatrix} + p\,\boldsymbol{n} = \kappa\,\boldsymbol{n}. \tag{2.6d}$$

The kinematic condition reads

$$v_r n_r + v_z n_z = V_f. \tag{2.6e}$$

The non-slip conditions can be expressed as

$$v_z = \Lambda_0 \exp(t), \quad v_r = -\tfrac{1}{2}r \quad \text{on } \Gamma_m, \tag{2.6f}$$

$$v_z = 0, \quad v_r = -\tfrac{1}{2}r \quad \text{on } \Gamma_s. \tag{2.6g}$$

To close the system, initial conditions for $\boldsymbol{v}$ and for the initial fluid bridge $\Omega(0)$ are prescribed, see § 4.2.

Remark 1. *The situation described above refers to an ideal geometry, where for instance the radii of the two membranes and their time evolutions are equal. In practice, however, owing to experimental imprecision the radii and their time-dependence may differ slightly. Therefore, in order to compare the numerical simulations with the experiments most accurately we prescribe functions $R_s(t)$, $R_m(t)$ with data taken from the experiments, see also* § 4.2.

3. Numerical method

Discretizing (2.6), the free boundary conditions (2.6*d*)–(2.6*e*) cause several problems, in particular, the treatment of the curvature terms and in finding a stable and efficient time discretization.

To resolve these problems we use a variational formulation, where the free-boundary condition (2.6*d*) is transformed to a boundary integral part of the bilinear forms. In the following, we sketch the basic ideas only; for further details see Bänsch (2001).

To proceed, we write the momentum part of the Stokes equations (analogously for the Navier–Stokes equations) in the strong form, multiply by a solenoidal test function $\boldsymbol{\varphi}$ vanishing on the no-slip parts Γ_s, Γ_m of the boundary and integrate by parts. We obtain

$$\int_{\Omega} \{-Ca\, \Delta \boldsymbol{v} + \nabla p\} \cdot \boldsymbol{\varphi} = 2Ca \int_{\Omega} D(\boldsymbol{v}) : D(\boldsymbol{\varphi}) - \int_{\Omega} p \nabla \cdot \boldsymbol{\varphi} - \int_{\Gamma_f} \boldsymbol{n} \cdot \boldsymbol{\sigma} \cdot \boldsymbol{\varphi},$$

where

$$D(\boldsymbol{v}) : D(\boldsymbol{\varphi}) := \sum_{i,j} D(\boldsymbol{v})_{i,j} D(\boldsymbol{\varphi})_{i,j}.$$

From the boundary condition (2.6d), we have

$$-\int_{\Gamma_f} \boldsymbol{n} \cdot \boldsymbol{\sigma} \cdot \boldsymbol{\varphi} = \int_{\Gamma_f} \kappa\, \boldsymbol{n} \cdot \boldsymbol{\varphi},$$

while a basic identity from differential geometry gives

$$\int_{\Gamma_f} \kappa\, \boldsymbol{n} \cdot \boldsymbol{\varphi} = \int_{\Gamma_f} \underline{\nabla} \boldsymbol{x} \cdot \underline{\nabla} \boldsymbol{\varphi}, \tag{3.1}$$

where $\underline{\nabla}$ is the tangential gradient on Γ_f and $\boldsymbol{x}$ the position vector.

Summarizing, we have

$$\int_{\Omega} \{-Ca\, \Delta \boldsymbol{v} + \nabla p\} \cdot \boldsymbol{\varphi} = 2Ca \int_{\Omega} D(\boldsymbol{v}) : D(\boldsymbol{\varphi}) - \int_{\Omega} p \nabla \cdot \boldsymbol{\varphi} + \int_{\Gamma_f} \underline{\nabla} \boldsymbol{x} \cdot \underline{\nabla} \boldsymbol{\varphi}. \tag{3.2}$$

Since the problem is axisymmetric, the above boundary integral can be expressed in parametric form as follows. Let Γ_f be given in parametric form by $\Gamma_f := \{r(s)\boldsymbol{e}_r + z(s)\boldsymbol{e}_z \mid s \in S\}$ with some parameter domain $S \subseteq I\!R$. Then for vector fields $\boldsymbol{f}, \boldsymbol{h}$

$$\int_{\Gamma_f} \underline{\nabla} \boldsymbol{f} \cdot \underline{\nabla} \boldsymbol{h} = \int_S \left\{ \frac{Q(s)}{r(s)} f_r h_r + \frac{r(s)}{Q(s)} (\partial_s f_r \partial_s h_r + \partial_s f_z \partial_s h_z) \right\} \mathrm{d}s$$

with $Q(s) := \sqrt{\partial_s r(s)^2 + \partial_s z(s)^2}$.

Although in our case a graph representation of the free surface Γ_f would be convenient, the above parametric form allows more general free surfaces to be considered.

Time discretization

To discretize in time a semi-implicit coupling of the unknowns for the geometry Ω and the flow variables $\boldsymbol{v}, p$ is used. More precisely, given the values Ω^{k-1}, $\boldsymbol{v}^{k-1}$, p^{k-1} at the discrete time instant t_{k-1}, we compute

Step 1: $\boldsymbol{v}^k$, p^k by solving (2.6a)–(2.6c) with boundary conditions (2.6d), (2.6f)–(2.6g) in Ω^{k-1},

Step 2: Γ_f^k by a discretized form of (2.6e): $\Gamma_f^k := \Gamma_f^{k-1} + (t_k - t_{k-1})\, \boldsymbol{v}^k$,

Step 3: Γ_m^k by (2.5) and also the update of the domain by an extension of Γ^k into the interior, resulting in Ω^k.

In Step 1, the boundary condition (2.6d) is incorporated via the variational formulation according to (3.2). The curvature terms are treated in a semi-implicit way using the identity $\boldsymbol{x}^k = \boldsymbol{x}^{k-1} + (t_k - t_{k-1})\boldsymbol{v}^k$ of Step 2 with $\boldsymbol{x}^{k-1}, \boldsymbol{x}^k$ the position

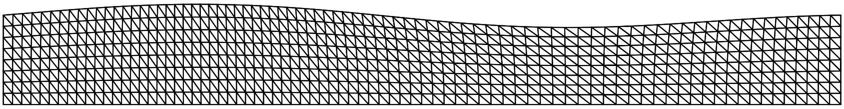

FIGURE 2. Typical (fine) triangular mesh with 1280 elements and 2737 velocity nodes.

vectors of Γ_f^{k-1}, Γ_f^k, respectively, i.e.

$$\int_{\Gamma_f^{k-1}} \underline{\nabla} \boldsymbol{x}^k \cdot \underline{\nabla} \boldsymbol{\varphi} = \int_{\Gamma_f^{k-1}} \underline{\nabla} \boldsymbol{x}^{k-1} \cdot \underline{\nabla} \boldsymbol{\varphi} + (t_k - t_{k-1}) \int_{\Gamma_f^{k-1}} \underline{\nabla} \boldsymbol{v}^k \cdot \underline{\nabla} \boldsymbol{\varphi},$$

which decouples the flow computation from the determination of the geometry. The above algorithm leads to an unconditionally stable and efficient treatment of the free boundary conditions, see Bänsch (2001).

For the extension of Γ^k into the interior in Step 3, a smoothing of the triangulation by a discrete Poisson equation is used.

The computation of $\boldsymbol{v}^k$, p^k is based on the axisymmetric version (Tenhaeff 1997) of the method and implementation described in Bänsch (1991, 1998). The underlying code uses the fractional step θ-scheme with operator splitting as variant, which decouples two major numerical difficulties, the solenoidal condition and the non-linearity (see Bristeau, Glowinski & Periaux 1986). The axisymmetric code solves for the unknowns (v_s, v_z) and p, where $v_s := v_r/r$. This scaling resolves the singularities of the operators at $r = 0$, and may be interpreted as a proper variational formulation of the axisymmetric Navier–Stokes equation in appropriately r-weighted Sobolev spaces (see also Lailly 1976).

Spatial discretization

To discretize in space the Taylor–Hood element, i.e. piecewise quadratic globally continuous elements for $\boldsymbol{v}$ and piecewise linear globally continuous elements for p, are used on triangular grids.

Some care must be taken in dealing with the rather large aspect ratios encountered during stretching. To this end, we use meshes that are condensed in the z-direction initially. Moreover, while moving the mesh from one time step to another, a smoothing operator maintains mesh regularity, see above.

Code validation

The code was validated with examples for Newtonian fluids from Zhang, Padgett & Basaran (1996) and Yao & McKinley (1998). Furthermore, the examples in § 5 were computed using several different meshes and time-step sizes to ensure that the discretization error was sufficiently small.

It may be noteworthy that, because of the higher spatial approximation order of the Taylor–Hood element and the accurate approximation of the curvature terms, only rather coarse meshes were needed. More precisely, it would have been sufficient to compute on meshes with 320 elements and using a (non-dimensional) time step $\delta t = 0.005$. To be on the safe side for the results presented in this paper, we used finer meshes with 1280 elements and a time step $\delta t = 0.0025$. Figure 2 shows a typical mesh with 1280 elements and 2737 velocity nodes.

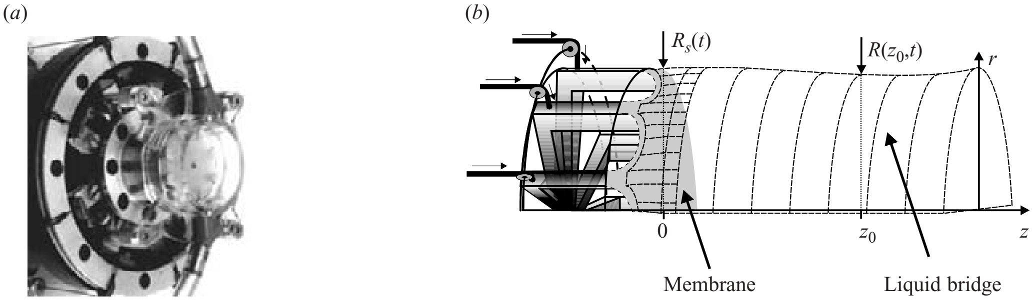

FIGURE 3. Membrane with time-dependent radius to adjust to the actual bridge length; (*a*) apparatus and (*b*) sketch of the device. The accelerated end moves in the z-direction, i.e. the direction where the device is dropped.

4. Experimental approach

4.1. *Set-up and procedure*

Extensional flows were experimentally achieved by stretching a large cylindrical liquid bridge. The bridge had sufficiently large dimensions to enable measurement of its extensional viscosity by the forces at the endplates, as done by Berg *et al.* (1994), or to carry macroscopic particles such as fibres or emulsion droplets for orientation and deformation experiments, performed by Berg (2002). The goal here was to generate a maximum homogeneous flow field with constant extension rates in space and time during stretching. For this reason, some technical effort was necessary to provide optimal flow conditions.

The stretching of the liquid bridge was performed under microgravity at the drop tower of Bremen. The microgravity environment during stretching was necessary to eliminate forces created by the hydrostatic pressure, see also the comment on the influence of non-vanishing gravitational forces at the end of § 5.3. The overall time for an experimental run under microgravity was determined by the height of the drop tower, resulting in 4.7 s for the Bremen experiments.

The liquid bridge was held between two almost circular concentric membranes, which stretched the liquid by time-controlled acceleration. The core of the apparatus comprised two membrane-reduction devices, each consisting of eight segments (see figure 3) to adjust the membrane radius $R(t)$ to the instantaneous length $L(t)$ of the liquid bridge according to (1.2), (1.3). To this end, the segments were connected to a stepping motor by thin wires, see figure 3(*b*). The lower (on the right hand side in our figures) device was fitted to a linear slider whereas the upper one had a fixed position. Before the start of the experiment, these membranes (together with two supporting PMMA cylinders) enclosed a volume of cylindrical shape. This volume was filled with fluid under 1g conditions. A sealing compound was necessary to insulate the device at the edge between the lower membrane and a cylindrical oil scraper.

The experiment was begun in the following way. After dropping the device (and hence under microgravity conditions) the rings were pulled away. To minimize losses and disturbances due to wetting of the supporting cylinders, those had been first coated with FC724 from 3M. Furthermore, the oil scraper was used for dewetting the opening supporting cylinders. Before starting the extension of the liquid bridge, the system was relaxed for 1 s, allowing initial perturbations induced by the movements of the rings to be sufficiently damped. The bridge extension was then started.

	$\mu\,(\mathrm{Pa\,s})$	$\gamma\,(10^{-3}\,\mathrm{N\,m^{-1}})$	$\rho\,(\mathrm{kg\,m^{-3}})$	$\dot{\epsilon}_0\,(\mathrm{s^{-1}})$	Λ_0	τ	Ca	We
Liquid 1	0.71	35.7	954	0.6	2	0.115	0.179	0.0325
Liquid 2	9.7	21.3	975	0.6	2	0.151	4.099	0.0556

TABLE 1. Characteristics of the fluids (at 25 °C): μ is the dynamical viscosity, γ the coefficient of surface tension, ρ the density; geometrical quantities: $\dot{\epsilon}_0$ is the stretching rate, Λ_0 the initial aspect ratio, τ the (dimensionless) relaxation time, see (4.1); dimensionless parameters: Ca, We are the capillary and Weber numbers, respectively.

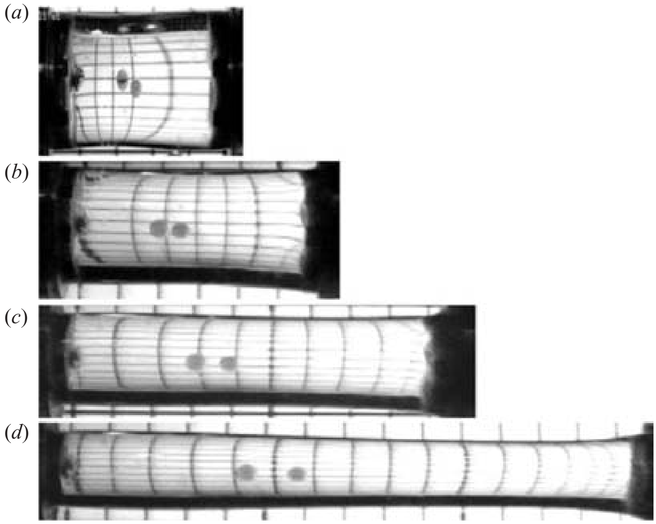

FIGURE 4. Initial and stretched bridge of castor oil liquid 1 at (a) $t = 0$, (b) $t = 0.444$, (c) $t = 0.888$, (d) $t = 1.344$, respectively; time in dimensionless units.

The initial size of the liquid bridge was 30 mm in length and 15 mm in radius. Modification of the radius was possible down to a minimum of 5 mm for a fluid length of 270 mm. The stretching rate was $\dot{\epsilon}_0 = 0.6\,\mathrm{s}^{-1}$ in our experiments.

Results from a typical experimental run, using castor oil (see table 1) in this example, are presented in figure 4. Figure 4(a) shows the liquid bridge before the onset of stretching, where the bridge is held between the membranes under microgravity conditions. The bridge is almost cylindrical before stretching and two immiscible emulsion droplets were placed inside the bridge to investigate their deformations in extensional flow in this particular case.

In figures 4(b)–4(d), the device on the right-hand side stretches the bridge for 3.5 s with exponentially increasing velocity according to (1.2). Simultaneously, the membranes decrease their radii exponentially so that the fluid boundaries adapt to the actual bridge length.

During stretching, a small amount of necking close to the accelerated device can be seen, which, as we will show in § 5, is typical and caused mainly by inertia forces in this parameter range ($Ca = 0.179$, $We = 0.0325$).

4.2. *Experimental conditions*

In the microgravity environment, residual accelerations caused by experimental disturbances occurred in the range $10^{-6}\,g - 10^{-2}\,g$. According to the microgravity

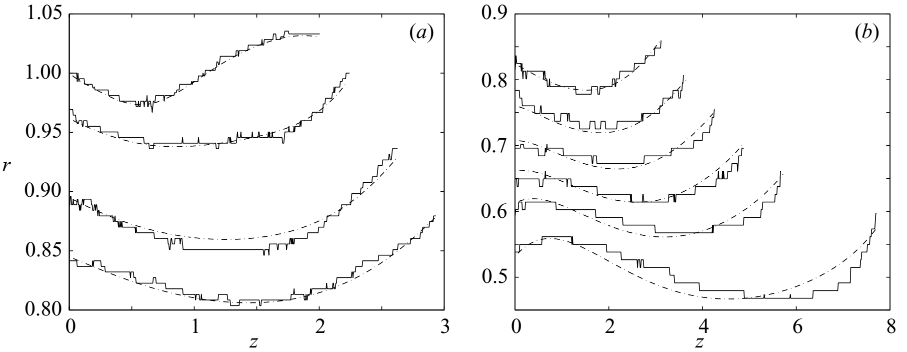

FIGURE 5. Liquid 1: bridge shape at time instants (*a*) $t = 0, t = 0.144$, $t = 0.288$, $t = 0.396$ and (*b*) $t = 0.444$, $t = 0.600$, $t = 0.744$, $t = 0.888$, $t = 1.04$, $t = 1.34$, from top to bottom, respectively; time in non-dimensional units; experiment (solid) and simulation (dash–dotted).

experiments of Berg (2002), disturbances greater than $10^{-6}\,g$ are irregular and damped out within less than 10^{-5} s. These short disturbances initiate waves from the membranes into the liquid bridge. However, owing to viscous dissipation, the waves are damped out within less than 0.1 mm and do not disturb the full bridge. Thus, only residual accelerations at about $10^{-6}\,g$ load the bridge with small hydrostatic pressure differences, characterized by Bond numbers Bo less than 10^{-4}. These small hydrostatic pressure differences were irrelevant in all experiments compared to capillary, viscous or inertia effects and were therefore neglected in the simulations. Note also that three-dimensional oscillations, which may disturb the bridges at small viscosity (see Higuera, Nicolás & Vega 2002), are not present in our configuration. This is because the bridge is held by supporting cylinders in the gravity phase, which inhibit such disturbances and provide a strictly axisymmetric start configuration, see also § 4.1.

Two different liquids with medium and high viscosity, respectively, were used in the experiments:

Liquid 1: castor oil, Lechner & Crebert GmbH, Mannheim, Germany,

Liquid 2: a highly viscous silicon oil, Dow Corning 200, Dow Chemical, USA; see also table 1 for properties of both liquids.

Both liquids enable almost cylindrical contours with small deformations to be maintained during stretching (see figure 4). The resulting differences in deformation between the two liquids were mainly caused by the different capillary numbers for liquid 1 and liquid 2.

For a precise comparison between experiment and numerical simulation, the real, opposed to ideal, experimental boundary conditions were taken into account. Since the liquid bridges were held exclusively by the membranes, the shape of the membranes determined the liquid boundaries Γ_s, Γ_m. The areas of the membranes and a small part at the sides of the membranes were wetted by the liquid without a sharp edge. Moreover, remnants of the sealing compound that was used to insulate the device (which had to be closed under $1g$ conditions before the experimental run), were attached to the moving membrane resulting in an increased effective radius. Therefore, the actual liquid radii $R_s(t)$ of Γ_s and $R_m(t)$ of Γ_m at the membrane positions during stretching were measured and imposed as boundary conditions in the numerical simulations instead of (2.4) and (2.5).

Moreover, the experimental procedure to provide the initial liquid bridges lead to concave–convex shaped contours (figures 5 and 6). Also, small losses of liquid from

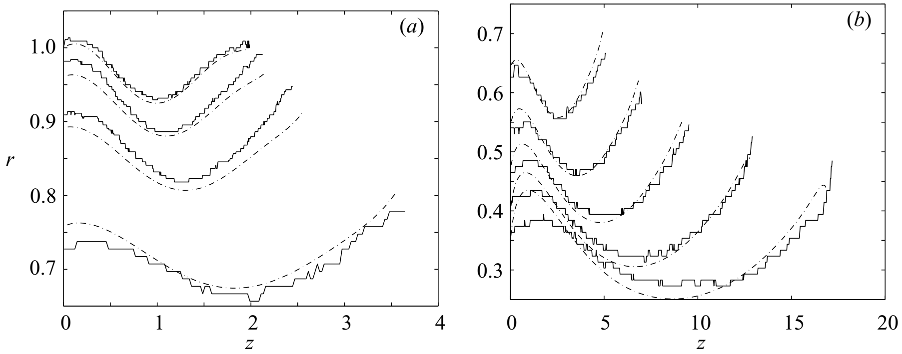

FIGURE 6. Liquid 2: bridge shape at time instants (*a*) $t = 0$, $t = 0.144$, $t = 0.288$, $t = 0.576$ and (*b*) $t = 0.888$, $t = 1.200$, $t = 1.488$, $t = 1.800$, $t = 2.064$, from top to bottom, respectively; time in non-dimensional units; experiment (solid) and simulation (dash–dotted).

the initial bridges could not be totally avoided; in fact, the initial liquid bridges only contained about 96% liquid volume of the ideal cylindrical bridge. The numerical simulations were thus started with the corresponding initial shapes, which were measured and then interpolated by a polynomial fit. The polynomial degree was optimized to obtain the best representation of the curves, resulting in the polynomial order 8 for liquid 1 and order 7 for liquid 2.

Furthermore, an initial rest state is incompatible with boundary conditions (2.6*f*), (2.6*g*), since this would give rise to a so called *impulsive* start, implying infinite acceleration forces initially.

In order to avoid this, we defined a start-up phase by imposing $\boldsymbol{v}(0,\cdot) = 0$ and defining the time-dependent boundary condition

$$v_z(t,\cdot) = \Lambda_0 \frac{\mathrm{d}}{\mathrm{d}t} \exp(t(1 - \exp(-t/\tau))) \quad \text{on } \Gamma_m, \tag{4.1}$$

which asymptotically approaches the ‘ideal’ function $v_z = \Lambda_0 \exp(t)$ on the time scale τ. The (dimensionless) relaxation time τ was fitted to measurements from the experiments (see Berg 2002) and the values for liquids 1 and 2 are given in table 1.

5. Results

5.1. *Comparison of experimental and numerical results*

As a first step in our investigation we compared the experimental results for liquid 1 and liquid 2 with corresponding numerical simulations. The experiments with liquid 1 and liquid 2 were performed for $0 \leqslant t \leqslant 1.344$ and $0 \leqslant t \leqslant 2.1$, respectively (non-dimensional units).

During the time evolution, the stretched bridges were recorded by a video camera with wide angle lens, allowing for total views of the bridge to a maximum length of 115 mm (liquid 1) and 245 mm (liquid 2), see figures 8 and 9. Moreover, a second camera provided a closer view of the accelerated bridges up to a time $t = 0.444$. The contours of the bridge surface were reliably determined by digital image processing, which identified the bridge shape by a strong gradient in the pixel brightness. Because of the different image resolutions of the two cameras (small and wide angle lenses), stronger pixel steps occur in the contour images for $t > 0.444$ (cf. figures 5 and 6).

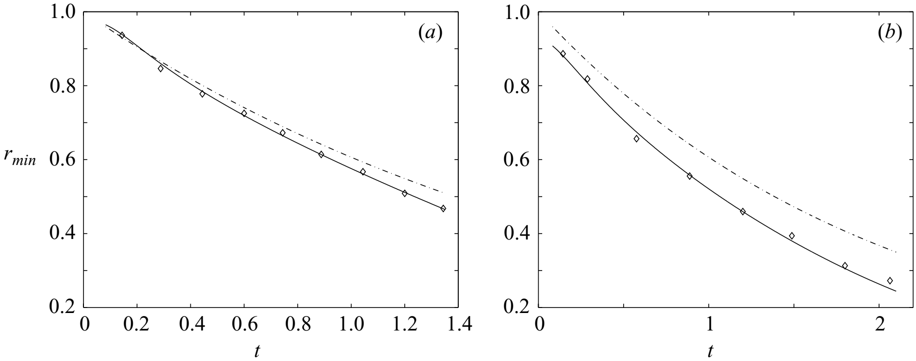

FIGURE 7. Minimum radius of the bridge versus time; experiment (diamonds), simulation (solid) and $\exp(-0.5\,t)$ (dashed–dotted); (*a*) liquid 1 and (*b*) liquid 2.

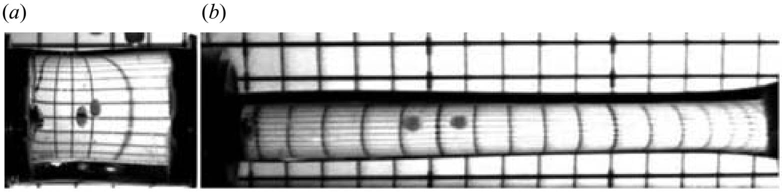
(*a*) (*b*)

FIGURE 8. Initial and stretched bridge of castor oil (liquid 1) at (*a*) $t = 0$ and (*b*) $t = 1.344$, respectively; time in dimensionless units.


(*a*) (*b*)

FIGURE 9. Initial and stretched bridge of silicon fluid (liquid 2) at (*a*) $t = 0$ and (*b*) $t = 1.344$, respectively; time in dimensionless units.

The transient bridge deformation during stretching can be subdivided into two parts. In the first time period, the capillary pressure tries to stabilize the bridge contour to a cylindrical shape of constant mean curvature. A first rough estimate of this time interval is determined by the stability limit of a stationary liquid bridge, i.e. the aspect ratio $\Lambda(t) = L(t)/R(t) \leqslant 2\pi$, which was studied by Plateau (1863) and Rayleigh (1878).

During this period, the initial deformation reorientates and relaxes, delayed by viscous forces. In the case of liquid 1, the deformation changes from a concave–convex shape to a purely concave shape. Moreover, capillary forces stabilize the bridge contour, counteracting the dynamic pressure difference caused by the acceleration of the flow.

Beyond the stability limit, in the remaining stretching period, the capillary and the dynamic pressures deform the bridge contour. A significant convex–concave deformation owing to the accelerated moving membrane arises. This type of bridge contour appears during stretching because of the negative pressure gradient in the vicinity of the accelerated membrane. The typical convex–concave shape is clearly visible in figure 5. Eventually, instability leads to a breakup of the bridge.

These two deformation processes, first reorientation by capillary pressure and then deformation by capillary and dynamic pressure differences, are clearly visible for liquid 1. Both processes also occur for liquid 2. However, because of its higher viscosity, the reorientation and convex–concave deformation are more delayed and the transition between the two phases is less pronounced.

The numerical simulations are capable of reliably describing the transient deformation during the bridge stretching of liquids 1 and 2. Figures 5 and 6 show that, in view of the real initial fluid volume and the measured membrane radii $R_s(t)$ and $R_m(t)$, the numerical results are in fairly good agreement with the experimental contours. More precisely, the experimental uncertainty of the recording device is 2 pixels and the agreement of the numerical results is of the same order of magnitude over most parts of the bridge and at almost all times.

Since the bridge stretches with exponentially increasing velocity and the deformations are also growing in time, differences between simulated and experimental data are expected to increase with time. The small difference maintained between numerical and experimental data at nearly all times is an indication of the quality of the numerical method.

A parameter commonly used to characterize the bridge deformation is the minimum radius of the deformed bridge versus time, shown for our examples in figure 7. There, the radii values (experimental as well as numerical) are compared to the ideal case of $R(t) = \exp(-0.5\,t)$. The deviation from the given exponential form characterizes the bridge deformation. Figure 7 confirms the reliability of the numerical results, demonstrating the good agreement of the minimum radius prediction with the experimental data.

From the sound numerical simulation of the transient bridge deformations in figures 5, 6 and 7, we can deduce that the capillary, inertia and viscous forces during reorientation and deformation are also accurately captured. In the next section, we discuss various parameter ranges, where the forces acting in a stretched liquid bridge and the corresponding bridge shapes are identified.

5.2. *Parameter variations and bridge shapes*

We used the numerical method described in § 3 to investigate bridge stretching and the corresponding flow quality for a wide variety of capillary and Weber numbers (shown in figure 10 with the cases numbered 1–30). The parameters were chosen to represent the bridge stretching at realistic fluid properties and bridge dimensions.

The initial aspect ratio Λ_0 was chosen to be 2 and the relaxation time τ, defined in (4.1), was set to $\tau = 0.012$ for all examples.

Since no data or rationale for choosing realistic, perturbed boundary conditions were available in the large parameter field, we imposed the ideal form (2.4), (2.5) and (2.6f), (2.6g) of the boundary conditions for the simulations.

Likewise, the initial bridge shape was chosen to be cylindrical (i.e. ideal). Robustness of the results with respect to perturbation of the initially cylindrical shape are discussed in § 5.4.

Physically, the parameter field can be interpreted in the following way: fixing the initial bridge radius to $R_0 = 15\,\mathrm{mm}$, the stretching rates are varied between $0.1\,\mathrm{s}^{-1}$ and $10\,\mathrm{s}^{-1}$. The surface tension and viscosity are varied in the ranges 20–70 $\mathrm{mN\,m}^{-1}$ and 0.001–1000 Pa s, respectively, while keeping the density constant at about $1000\,\mathrm{kg\,m}^{-3}$,

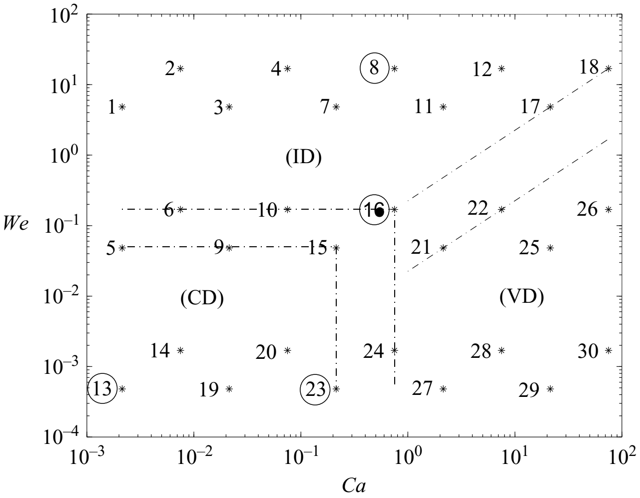

FIGURE 10. Parameter field, numbering of the numerical experiments; the dash-dotted lines mark the respective transition regions between capillary-dominated (CD), viscous-dominated (VD) and inertia-dominated (ID) flows. Ringed examples 8, 13, 16 and 23 are discussed in detail in the text.

Number	Liquid	μ (Pa s)	γ (10^{-3} N m^{-1})	ρ (kg m^{-3})	$\dot{\epsilon}_0$ (s^{-1})	$t_{breakup}$ (s)
1	Water	0.001	72	998	10	0.05
13	85% Glycerol–water	0.1129	66	1123	0.09	12
18	Silicon liquid	10	21	975	10	0.23
30	Silicon liquid	1025	21	976	0.1	60

TABLE 2. Some physical liquids in the parameter field. The last column shows the approximate lifespan $t_{breakup}$ of the bridges obtained from the computations in § 5.2.

(cf. table 2, where some possible physical liquids are identified within the parameter field).

Anticipating the result of our study, the parameter field can be subdivided into three major regimes:

(i) *capillary-dominated flow*, characterized by $Ca \ll 1$, $We \ll 1$,

(ii) *viscous-dominated flow*, $Ca > O(0.1)$, $Re < O(0.1)$,

(iii) *inertia-dominated flow*, $We > O(0.1)$, $Re > O(0.1)$.

The field could be extended considerably to other bridge dimensions and strain rates, but systematic changes of the flow quality and the deformation behaviour are expected only at the transition between the capillary-, viscous- or inertia-dominated flow regimes, respectively.

A first overview of the situation is given in figure 11, which presents the minimum radii of the stretched bridges for various Weber and capillary numbers, as well as the 'ideal' exponential curve denoted 'e' for comparison. The figures clearly confirm the transitions between the different flow regimes.

Figure 11 shows the transition from almost capillary-dominated flow states to flow states determined by viscosity (figures 11*a*) or inertia (figures 11*b*).

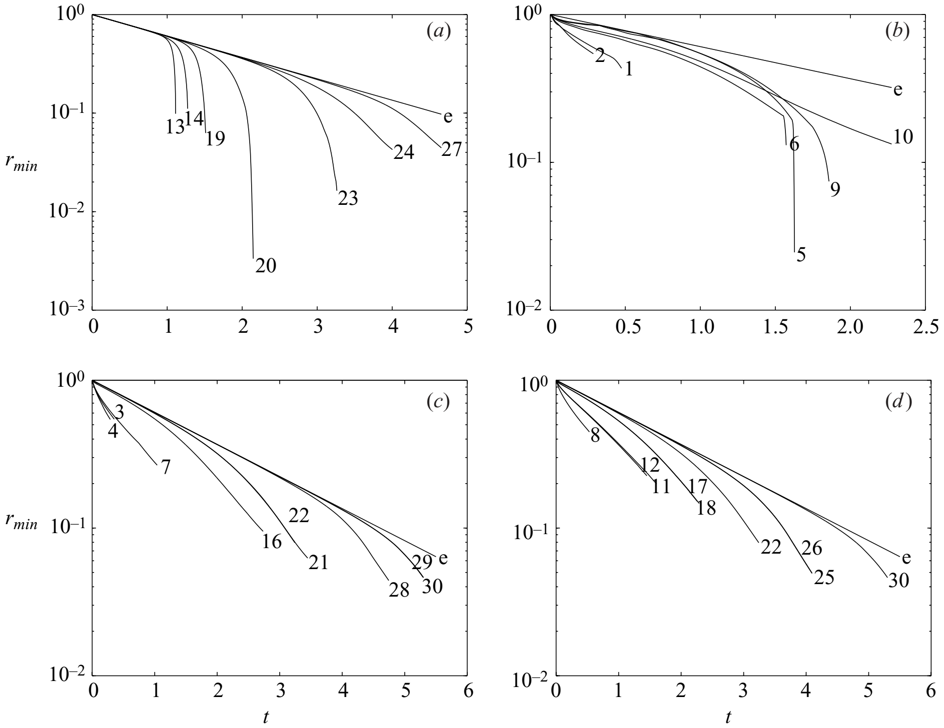

FIGURE 11. Minimum radii of the bridges versus time.

At low capillary and Weber numbers (numbers 13, 14, 19, 20, 23), the minimum bridge radii coincide with the ideal exponential function up to the capillary stability limit. Beyond this limit, capillary instability leads to distortion of the bridge and the final breakup. The larger the capillary number and the smaller the Weber number, the longer the lifetime of the bridge. For minimal values of the capillary and Weber numbers (number 13), the bridge breaks up just after $t = 1.0$. For higher capillary numbers, the breakup is delayed.

Completely different behaviour can be seen for the transition from low capillary and Weber numbers (numbers 13, 14) to increased Weber numbers (numbers 1, 2, 5, 6). Whereas at small Weber numbers (numbers 13, 14) the minimum bridge radii stay relatively close to the ideal exponential function during their whole life span, the radius functions at higher Weber numbers (numbers 1, 2, 5, 6) deviate from the exponential function from the start. The lifetime of a bridge decreases, and the deviation to the ideal case increases with increasing Weber number. The extreme examples (numbers 1, 2) are strongly deformed and short-lived bridges.

REMARK 2. *Some of the bridges are strongly deformed from the start, yielding rather distorted meshes in the numerical simulations despite the mesh smoothing in Step 3 of the algorithm, see* § 2. *This gives rise to a shorter 'numerical' rather than physical life span of the corresponding bridges.*

Figures 11(*a*) and 11(*b*) show the influence of decreasing Weber number and increasing capillary number. It can be seen that for higher values of $Re = We/Ca$

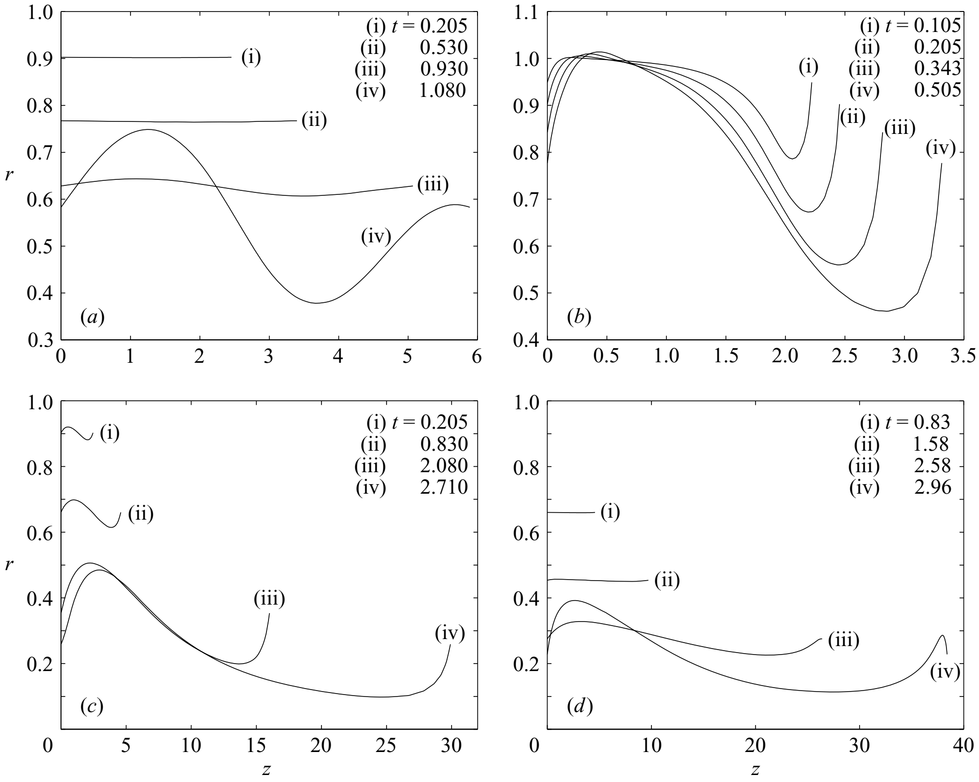

FIGURE 12. Bridge shapes for some representative examples. (*a*) Example 13 represents capillary-dominated flow. (*b*) Example 8 represents inertia-dominated flow. (*c*) Example 16 represents the transition from capillary- to viscous-dominated flow. (*d*) Example 23 represents the transition from inertia to viscous-dominated.

(numbers 3, 4, 7, 8, 11, 12, 16, 17, 18, 21) the minimum bridge radii are not at all close to the ideal exponential function. The deviation from the ideal case increases with increasing Reynolds number. On the other hand, at lower Reynolds numbers, the minimum bridge radius is close to the ideal case and the breakup is more delayed.

Moreover, it is noteworthy that the curves of minimum bridge radii are nearly identical for identical Reynolds numbers (numbers 11/12, 17/18, 21/22, 25/26, 29/30). This shows that capillary forces do not have a strong influence on the deformation behaviour at higher capillary or Weber numbers, $Ca > 0.75$ or $We > 0.17$, i.e. outside the capillary-dominated regime.

In the rest of this section we discuss four representative examples, bridge numbers 13, 8, 16 and 23, from capillary to inertia and then viscous-dominated flow in more detail. The respective contour shapes of these bridges for several time instants are plotted in figure 12.

Bridge 13 at $Ca = 2.14 \times 10^{-3}$ and $We = 4.82 \times 10^{-4}$ represents capillary-dominated flow. After the start and during the main part of the stretching period, represented by the instants $t = 0.205$, $t = 0.53$, respectively, a nearly ideal (cylindrical) shape exists. After this, the capillary instability induces a convex–concave shape leading to the final breakup of the bridge. The almost symmetric shape of the convex–concave distribution is an indication of the predominantly capillary-driven instability, which by linear stability analysis is predicted to take on a sinusoidal form.

Bridge 8 at $Ca = 7.50 \times 10^{-1}$ and $We = 1.69 \times 10^{1}$ represents inertia-dominated flow. As soon as the stretching begins, strong contour deformations develop close to the accelerated side. These disturbances are caused by the inertia of the liquid and are not significantly damped by viscous or capillary forces during stretching. The contour deformation remains until the breakup of the bridge.

Bridge 16 at $Ca = 7.50 \times 10^{-1}$ and $We = 1.69 \times 10^{-1}$ represents the situation of balanced viscous and capillary forces and smaller inertia forces. The bridge develops only small deformations during stretching compared to, for instance, bridge 8. As can be seen from figure 12 at $t = 0.205$, a tiny convex–concave deformation is visible, which grows slowly during stretching. The deformation is caused by the dynamic pressure difference and is compensated by the capillary pressure. The stronger viscous forces in comparison to inertia forces prevent strong local deformations and flow variations, as seen for instance in example number 8.

Bridge 23 at $Ca = 2.14 \times 10^{-1}$ and $We = 4.82 \times 10^{-4}$ shows an example of viscous-dominated flow. The higher viscous forces in comparison to example number 16 prevent strong local pressure variations inside the bridge and the bridge has a cylindrical shape during the main part of the stretching period. Just before the breakup a convex–concave deformation occurs.

5.3. *Strain and shear*

The evaluation of the strain and shear distribution inside the bridge provides a means of assessing the quality of the uniaxial extensional flows. In cylindrical coordinates, the strain rate $\dot{\epsilon}$ and the shear rate $\dot{\gamma}$ are given by

$$\dot{\epsilon} = \tfrac{2}{3}(\partial_z v_z - \partial_r v_r), \qquad \dot{\gamma} = \partial_r v_z + \partial_z v_r.$$

We are interested in the regions of Ω that are homogeneous with respect to the strain rate and shear rate. To this end we define the homogeneous part Ω_{hom} of Ω, where the deviation from the desired strain and shear rate distribution of the ideal bridge is less than 5%:

$$\Omega_{hom}(t) := \{x \in \Omega(t) \mid \max\{|\dot{\epsilon}(t,x) - 1.0|, |\dot{\gamma}(t,x)|\} < 0.05\}, \tag{5.1}$$

as well as the fraction of the homogeneous part

$$\mathrm{hom}(t) := \frac{|\Omega_{hom}(t)|}{|\Omega(t)|}. \tag{5.2}$$

The latter expression is a direct measure of the quality of a stretched bridge. Figure 13 indicates the time-dependence of *hom* for the given examples considered. For the sake of clarity some curves are omitted. The omitted curves are either close to those corresponding to neighbours in the parameter field or their values of *hom* are negligibly small for the whole stretching period (bridges 1, 2, 3, 4, 7, 8, 11, 12).

From figures 11 and 13 a clear correspondence can be seen between the flow quality, characterized by *hom*, and the bridge deformation, expressed by the function of minimum radius.

Comparison of the curves in figures 11(a) and 13(a) (examples 13, 20, 23, 27) shows that, as long as the minimum radius follows the ideal exponential function, i.e. there is no large deformation of the bridge, the flow inside the bridge enjoys a maximum homogeneity *hom*, which in turn implies that the shear is minimum.

In the range of capillary-dominated flows (e.g. bridges 13, 20), the homogeneous fraction vanishes just at the onset of the breakup of the bridge.

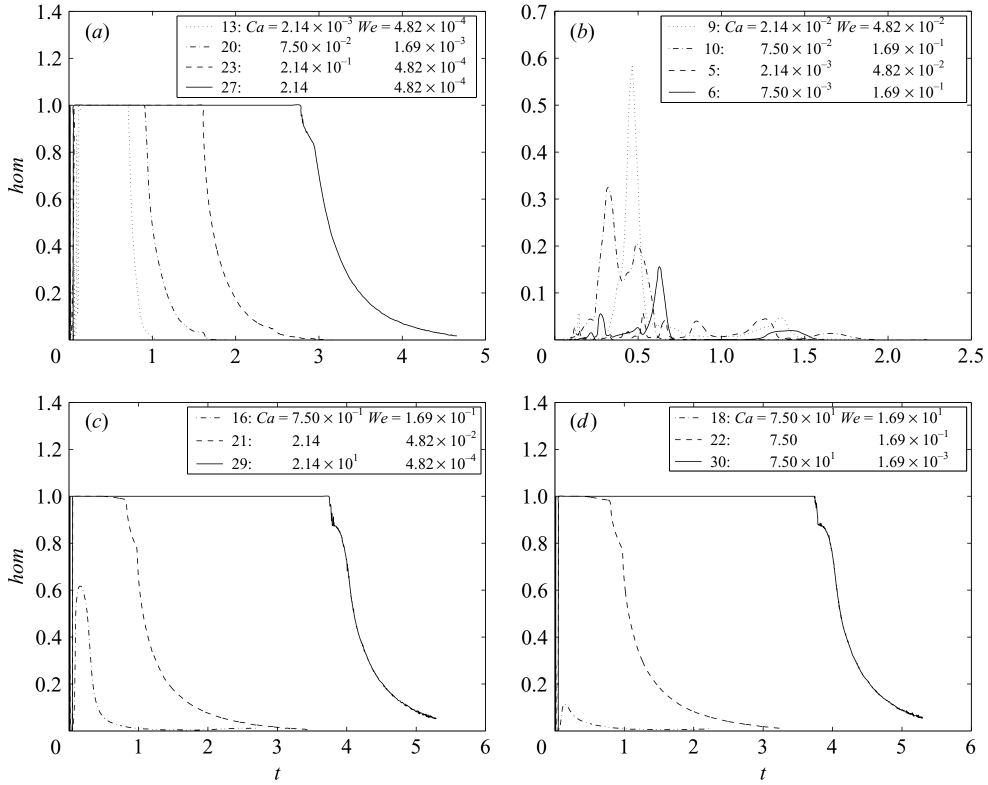

FIGURE 13. Homogeneous fraction of the domain $\mathrm{hom}(t) := |\Omega_{hom}(t)|/|\Omega(t)|$ for the examples in the parameter field.

For higher Weber numbers (numbers 5, 6, 9, 10), the bridge contours behave similarly to example 16 in figure 12, exhibiting a convex–concave shape during stretching. These asymmetrical deformations result in relatively small homogeneous fractions compared to those for lower Weber numbers.

For viscous-dominated flows (22, 29, 30), the homogeneous fraction is maximal and the shear rates are minimal. This is caused by the strong viscous transport of momentum, which inhibits strong deformations and flow variations; hence the deformations are small and the bridge follows the ideal exponential case. On the other hand, for inertia-dominated flows (7, 8, 12, 18), the strong dynamic pressure gradients cause strong deformations and flow variations, resulting in large shear rates. The homogeneous fractions for these examples are extremely small. In the case of experiments 7, 8, 12, the homogeneous flow fraction remains close to zero and is therefore not displayed in figure 13.

To summarize, viscous- and inertia-dominated flows exhibit very strong differences in the flow quality, expressed by the homogeneous fraction *hom*. Hence, the best regime in terms of quality of the underlying extensional flow field is viscous-dominated flow at small Reynolds numbers. We note, however, that in the case of small capillary numbers, as well as small Reynolds numbers, where capillary forces dominate, the extensional flow is remarkably homogeneous up to the point of capillary-driven breakup.

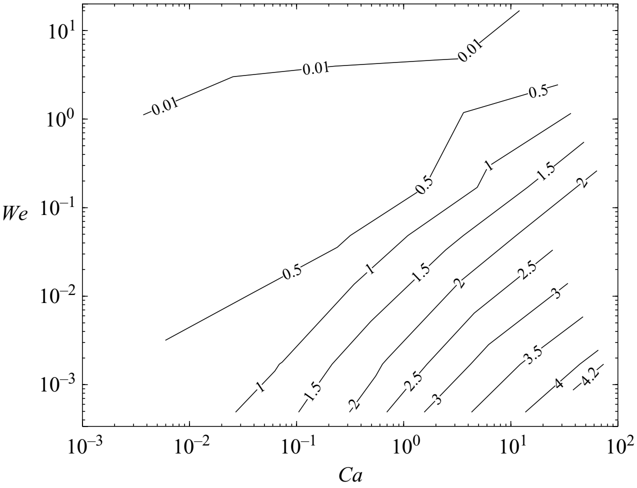

FIGURE 14. Contour plot of the quality measure *qual*, defined by (5.3).

It should also be mentioned (without showing the corresponding curves) that the shear rate is related to *hom*, i.e. the shear rate is high when *hom* is small, and vice versa.

In order to obtain an even more condensed measure for the bridge qualities, we define the scalar quantity *qual*,

$$qual := \int_0^{t_{breakup}} \mathrm{hom}(t)\,\mathrm{d}t. \tag{5.3}$$

This demonstrates increasing flow quality at decreasing Weber numbers and increasing capillary numbers, cf. figure 14. Large values of *qual* indicate the desirable situation of a large homogeneous flow fraction during a long time period.

Interestingly, *qual* remains almost constant at constant Reynolds numbers in the *We–Ca* parameter field. This behaviour is most clearly visible for higher capillary number, where capillary forces are negligible. In this range, *qual* is a decreasing function of the Reynolds number only.

Finally, we remark on the influence of possible inhomogeneities induced by gravity and non-adjusted disk radii. Computationally, we found that even small gravitational forces lead to very strong distortions of the bridges. Bond numbers as small as $Bo = 0.1$ (for capillary-dominated bridges) to $Bo = 10$ (for viscous-dominated bridges) already give rise to bridges having no significant homogeneous fraction. Note that for typical bridge dimensions ($\rho = 1000\,\mathrm{kg\,m^{-3}}$, $\gamma = 30 \times 10^{-3}\ \mathrm{N\,m^{-1}}$, $R_0 = 15\,\mathrm{mm}$) the $1g$ situation implies a Bond number of $Bo = 75$.

Furthermore, fixing the radii of the endplates also destroys the quality of the flow fields for our Newtonian liquids. In this case, for all values of *Ca* and *We* in the parameter field, the obtained bridges were of lower quality regarding homogeneity.

Thus, we conclude that both the microgravity environment as well as the adjustments of the disk radii are crucial to produce high-quality flow fields.

5.4. *Sensitivity with respect to initial perturbations*

As seen in § 4.2, because of experimental difficulties, we cannot achieve ideal initial and boundary conditions. Therefore, the sensitivity of the computational results of

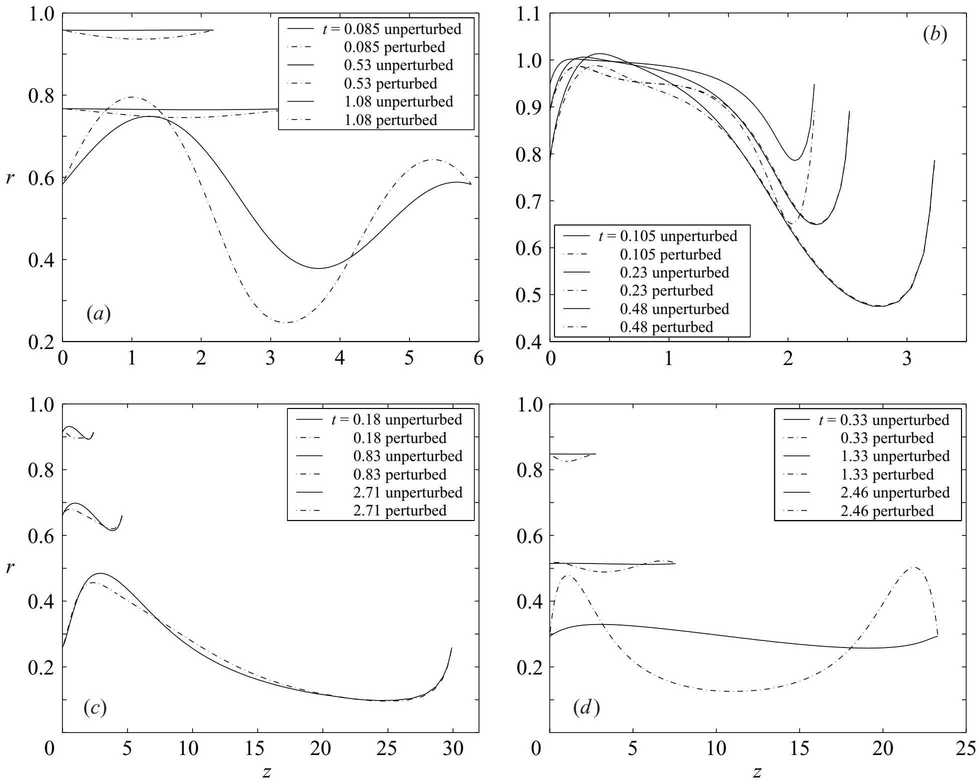

FIGURE 15. Bridge shapes for the representative examples (*a*) 13, (*b*) 8, (*c*) 16, (*d*) 23: contours for ideal initial bridges (solid lines) and perturbed initial bridges (dashed lines) at different time instants.

§ 5.2 is an important issue. If the results were too sensitive to perturbations, the above parameter study would be useless in practice.

To form an idea of the sensitivity, we compared stretching of the representative bridges 8, 13, 16, 23 with ideal and perturbed initial configurations.

To this end we performed simulations, where the initial configurations were taken from the experimental data of liquid 1, see § 4.2 and figure 5. The results are given in figure 15, showing the bridge shapes at various time instants and in figure 16 showing hom(t).

Bridge 16 behaves even better in the perturbed situation. The instability for this bridge develops as a strongly convex–concave shape, which is opposite to the concave–convex shape of the initial perturbation.

In general, the qualities of the perturbed bridges are still sufficiently close to the unperturbed ones, as to conclude that the results found in § 5.2 are stable with respect to these perturbations.

5.5. *Flow regimes and application*

In this section, we discuss in more detail the strain and shear distributions for the four examples, bridges 13, 8, 16 and 23, and give further details for applications.

I. Capillary-dominated flow, bridge 13. As seen above, even for small capillary numbers and small Reynolds numbers, homogeneous flow can be realized during almost the entire period of stretching. For instance, bridge 13 includes a homogeneous

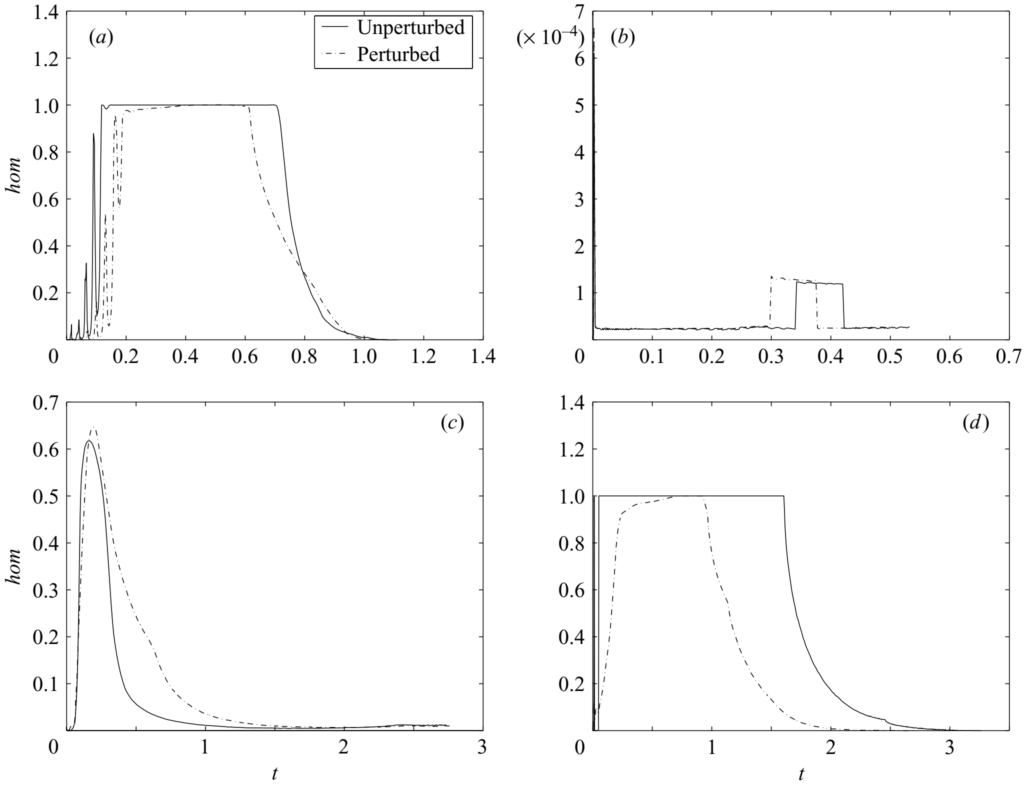

FIGURE 16. Homogeneous fraction $\mathrm{hom}(t) := |\Omega_{hom}(t)|/|\Omega(t)|$ of the domain for the representative examples (*a*) 13, (*b*) 8, (*c*) 16, (*d*) 23. Simulations start with ideal initial bridges (solid lines) and perturbed initial bridges (dashed lines), respectively.

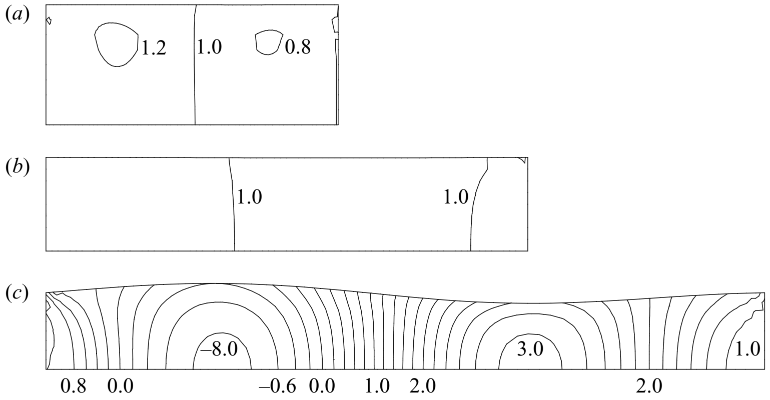

FIGURE 17. Bridge 13: strain rate distribution at (*a*) $t = 0.08$, (*b*) $t = 0.58$ and (*c*) $t = 0.98$; difference between successive isolines is 0.2.

strain flow immediately after the start: figures 17 and 18 show the strain and shear rate distribution inside this bridge at different time instants.

Just after the start (e.g. $t = 0.08$ in figure 17), viscous momentum transport from the membranes into the bridge causes a weak strain variation and a weak shear flow

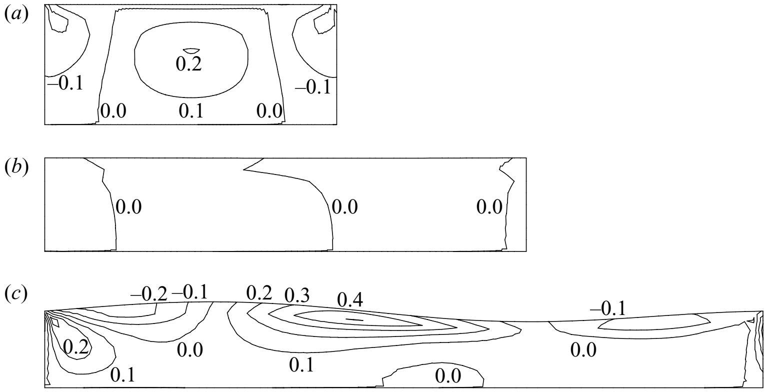

FIGURE 18. Bridge 13: shear rate distribution at (*a*) $t = 0.08$, (*b*) $t = 0.58$ and (*c*) $t = 0.98$; difference between successive isolines is 0.1.

fraction; these are damped down quickly by the capillary forces (which are strong compared to inertia and viscous forces).

During the main part of the stretching period, represented by the instant $t = 0.58$ for example, an ideal extensional flow prevails, until capillary forces initiate strong variations in strain and shear rates, (e.g. at $t = 0.98$), which then lead to the final capillary-dominated breakup.

As long as the bridge maintains an ideal cylindrical shape, the extensional flow is perfectly homogeneous inside the bridge. After this, the capillary instability induces a deformed shape, see figure 12. In the concave part of the bridge the strain rate increases, while in the convex part the strain rate decreases (see figures 17 and 18).

Eventually, at the end of the stretching period, strong variations in strain rate and high values of the shear rate lead to a 'quick-vanishing' *hom*, see figure 13.

We conclude that homogeneous strain experiments in the range of small Reynolds numbers and small capillary numbers are possible up to the capillary breakup stage.

II. Inertia-dominated flow at high Weber and capillary numbers, bridge 8. This bridge represents a less suited regime for homogeneous extensional flow. Figures 19 and 20 show the strain and shear rate distribution inside the bridge at different time instants.

As early as $t = 0.05$, strong flow variations have developed close to the accelerated side. Since viscous (diffusive) momentum transport inside the bridge is weak, the forces lead to a strong contour necking.

In the left-hand convex part of the bridge, the strain rate is well below the desired strain rate of unity. This example shows that dominant inertia at high Weber and capillary numbers precludes homogeneous strain flow.

III. Balanced viscous and capillary forces with small inertia forces, bridge 16. Studying bridge 16, we see that these parameters provide more suitable conditions for homogeneous extensional flow and is typical for bridges with a Reynolds number of 0.225.

Figures 21 and 22 show the strain and shear rate distribution inside the bridge at different time instants. The bridge develops only small flow variations during stretching.

Despite the better flow quality in comparison to example 8, figure 13 confirms that almost no homogeneous flow exists inside the bridge for the main part of the stretching period. However, since the flow variations are weak in the convex part,

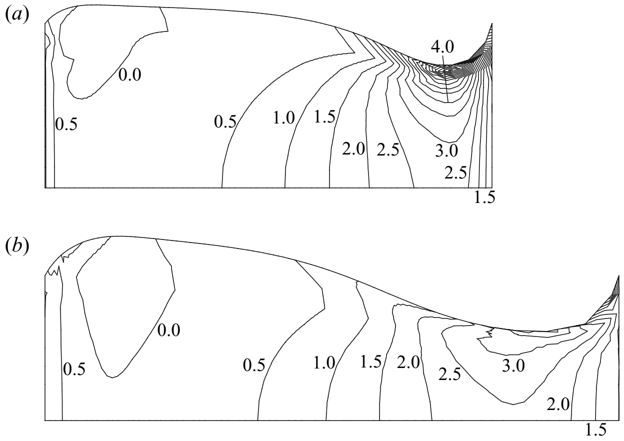

FIGURE 19. Bridge 8: strain rate distribution at (*a*) $t = 0.05$ and (*b*) $t = 0.455$; difference between successive isolines is 0.5.

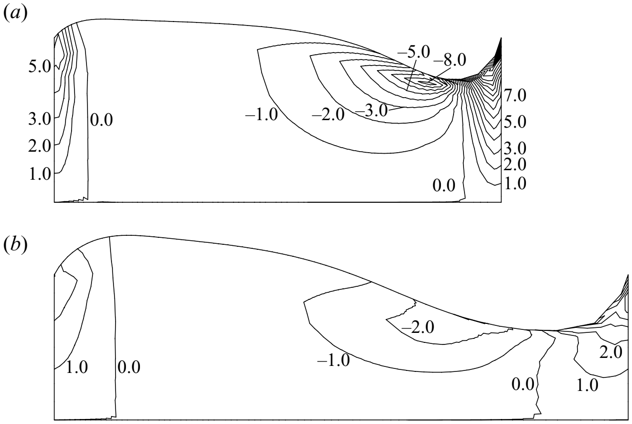

FIGURE 20. Bridge 8: shear rate distribution at (*a*) $t = 0.05$ and (*b*) $t = 0.455$; difference between successive isolines is 1.0.

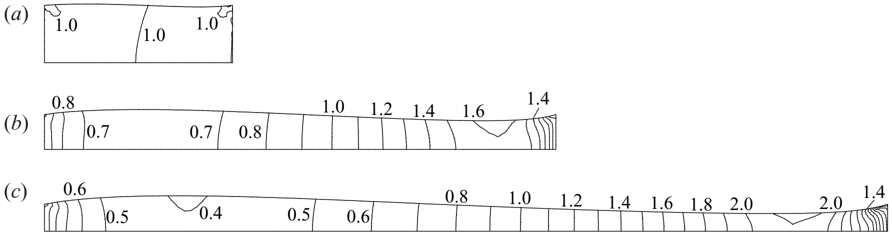

FIGURE 21. Bridge 16: strain rate distribution at (*a*) $t = 0.205$, (*b*) $t = 1.205$ and (*c*) $t = 1.705$; difference between successive isolines is 0.1.

a local shear-free strain flow exists for some time, which may be used for strain experiments.

IV. Low Weber numbers, medium capillary numbers, bridge 23. As mentioned above, the most suitable parameters for homogeneous extensional flow correspond to

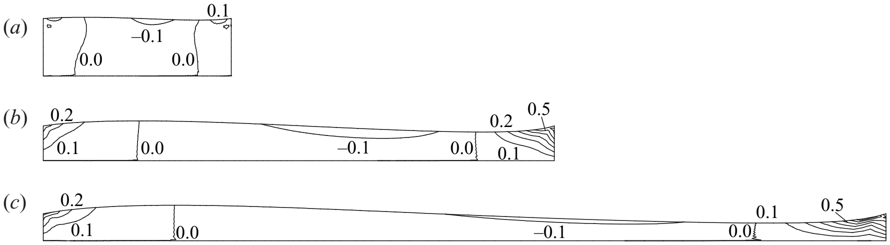

FIGURE 22. Bridge 16: shear rate distribution at (*a*) $t = 0.205$, (*b*) $t = 1.205$ and (*c*) $t = 1.705$; difference between successive isolines is 0.1.

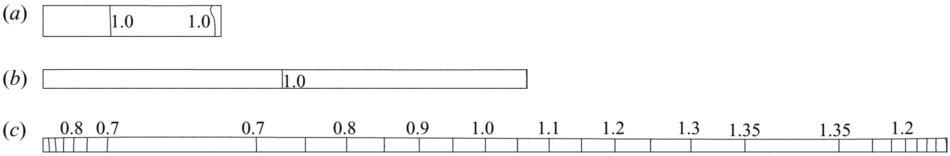

FIGURE 23. Bridge 23: strain rate distribution at (*a*) $t = 0.58$, (*b*) $t = 1.58$ and (*c*) $t = 2.205$; difference between successive isolines is 0.05.

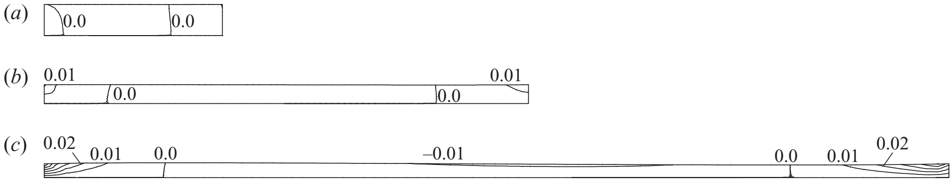

FIGURE 24. Bridge 23: shear rate distribution at (*a*) $t = 0.58$, (*b*) $t = 1.58$ and (*c*) $t = 2.205$; difference between successive isolines is 0.01.

viscous flows with small capillary forces. Such parameters at high capillary numbers and small Reynolds numbers are only realizable at very high fluid viscosity, which may not be available in the experiments.

Therefore, a more practical example (bridge 23) at medium viscosity or, in non-dimensional terms, medium capillary number is presented in figures 23 and 24.

The figures show the strain and shear rate distribution inside the bridge at different time instants. The higher viscous forces in comparison to those in the previous example prevent strong local pressure variations inside the bridge. Therefore, the bridge remains cylindrical and the flow homogeneous during the main part of the stretching period. Variations in the strain and shear rates appear just before the breakup.

The very weak flow variations demonstrate the excellent flow quality, which makes a bridge at low Reynolds number and even medium capillary number suitable for strain experiments.

Examples I–IV reveal that small inertia forces, in comparison to viscous and capillary forces, are necessary for the realization of homogeneous uniaxial extensional flow.

As outlined above, the parameter regime providing the most suitable conditions for continuous homogeneous extensional flow under conditions of negligible gravity is found to be for low Reynolds numbers and high capillary numbers. Unfortunately, these parameters cause certain difficulties in practice. High capillary numbers and small Reynolds numbers are only realizable at very small bridge dimensions and very high fluid viscosity. High viscosity causes severe difficulties in controlling the fluid, which makes it unrealistic in this context. Therefore, extensional flow experiments are mainly performed at medium or low capillary numbers, where the duration of homogeneous flow is limited in space and time.

Moreover, in the range of small Reynolds numbers as well as small capillary numbers, where inertia forces are smaller than viscous and capillary forces, the experimental realization of homogeneous extensional flows is indeed restricted by further difficulties. For instance the duration of the ideal homogeneous flow varies from case to case, cf. figure 13. The examples reveal that for decreasing capillary number, stronger capillary forces (compared to viscous forces) lead to a shorter lifetime for the homogeneous flow. This is also confirmed by the plot for minimum radii in figure 11, where the breakup time decreases with decreasing capillary number.

6. Conclusion

We have investigated the possibility of generating nearly homogeneous uniaxial extensional flows with an almost-constant strain rate in a stretched liquid bridge under microgravity conditions. The key ingredient of the method is the adjustment of the disk diameters in maintaining ideal boundary conditions in a cylindrical liquid bridge. This method gives rise to much weaker end-effects than the commonly used method with unchangeable disks.

However, even under these optimal conditions, the liquid bridges are deformed by forces arising from the fluid inertia and surface tension. The balances between inertia and surface tension forces, expressed by the Weber number, and between viscous and surface tension forces, expressed by the capillary number, determine the deformation and flow behaviour.

Our investigations systematically present different deformations and flow qualities depending on Ca, We and $Re = We/Ca$. Regions of *capillary-dominated flow*, $Ca \ll 1$, $We \ll 1$, *viscous-dominated flow*, $Ca > O(0.1)$, $Re < O(0.1)$, and *inertia-dominated flow*, $We > O(0.1)$, $Re > O(0.1)$ have been detected, which exhibit mutually different bridge deformations during stretching.

In the range of *capillary-dominated flow*, ideal extensional flows exist during the main part of the stretching period, until capillary forces initiate strong variations in strain and shear rates to the final capillary-dominated breakup. As long as the bridge maintains an (almost) ideal cylindrical shape, the extensional flow is (nearly) perfectly homogeneous inside the bridge. In the range of small capillary numbers and small Reynolds numbers, homogeneous strain experiments are possible up to capillary breakup. However, weak viscous forces (compared to capillary ones) do not essentially delay the capillary-dominated breakup. Therefore the period of ideal flow is limited in this case.

In the range of *inertia-dominated flow*, strong flow variations and contour deformations occur, which are caused by the fluid inertia and are not damped by viscous or capillary forces during stretching. This is the most unsuitable regime for homogeneous extensional flow.

The most suitable parameters for homogeneous extensional flow are in the range of *viscous-dominated flow*. The high viscous forces in comparison to inertia and capillary forces prevent strong local pressure variations inside the bridge. Therefore, the bridge remains cylindrical and the flow homogeneous and constant during a long stretching period. Moreover, in this range the flow quality is a decreasing function of the Reynolds number only.

In experiments, some parameters (high capillary numbers and small Reynolds numbers) may not always be realizable, because of the fluid properties or bridge geometry. In this case, we can make an estimate for the expected flow quality, expressed by the quantity *qual* depending on the parameters *Ca* and *We*, see for instance figure 14.

REFERENCES

Bänsch, E. 1991 An adaptive finite-element-strategy for the three-dimensional time-dependent Navier–Stokes equations. *J. Comput. Appl. Maths* **36**, 3–28.

Bänsch, E. 1998 Simulation of instationary, incompressible flows. *Acta Math. Univ. Comenianae* **67**, 101–114.

Bänsch, E. 2001 Finite element discretization of the Navier–Stokes equations with a free capillary surface. *Numer. Maths* **88**, 203–235.

Berg, C. P. 2002 Droplet deformation in uniaxial and plane extensional flow fields. PhD thesis, University of Bremen, Shaker (in German).

Berg, C. P., Dreyer, M. & Rath, H. J. 1999 A large fluid–bridge device to measure the deformation of drops in uniaxial extensional flow fields. *Meas. Sci. Technol.* **10**, 956–964.

Berg, S., Kröger, R. & Rath, H. J. 1994 Measurement of extensional viscosity by stretching large liquid bridges in microgravity. *J. Non–Newtonian Fluid Mech.* **55**, 307–319.

Bristeau, M. O., Glowinski, R. & Periaux J. 1986 Numerical methods for the Navier–Stokes equations. Application to the simulation of compressible and incompressible flows. *Comput. Phys. Rep.* **6**, 73–188.

Chin, H. B. & Han, C. D. 1979 Studies on droplet deformation and breakup. I. Droplet deformation in extensional flow. *J. Rheol.* **23**, 557–590.

Eggers, J. 1997 Nonlinear dynamics and breakup of free-surface flows. *Rev. Mod. Phys.* **69**, 865–929.

Gaudet, S., McKinley, G. H. & Stone, H. A. 1996 Extensional deformation of Newtonian liquid bridges. *Phys. Fluids* **8**, 2568–2579.

Higdon, J. J. L. 1993 The kinematics of the four-roll mill. *Phys. Fluids* A **5**, 274–276.

Higuera, M., Nicolás, J. A. & Vega, J. M. 2002 Weakly nonlinear nonaxisymmetric oscillations of capillary bridges at small viscosity. *Phys. Fluids* **14**, 3251–3269.

Kröger, R., Berg, S., Delgado, A. & Rath, H. J. 1992 Stretching behaviour of large polymeric and Newtonian liquid bridges in plateau simulations. *J. Non-Newtonian Fluid Mech.* **45**, 385–400.

Lailly, P. 1976 Numerical solution of the axisymmetric Stokes equations by a nonconforming finite element method. PhD thesis, Paris (in French).

McKinley, G. H. & Sridhar, T. 2002 Filament-stretching rheometry of complex fluids. *Annu. Rev. Fluid Mech.* **34**, 375–415.

McKinley, G. H. & Tripathi, A. 2000 How to extract the Newtonian viscosity from capillary breakup measurements in a filament rheometer. *J. Rheol.* **44**, 653–670.

Maia, J. M., Covas, J. A., Nóbrega, J. M., Dias, T. F. & Alves, F. E. 1999 Measure uniaxial extensional viscosity using a modified rotational rheometer. *J. Non-Newtonian Fluid Mech.* **99**, 183–197.

Matta, J. E. & Tytus, R. P. 1988 Liquid stretching using a falling cylinder. *J. Non-Newtonian Fluid Mech.* **30**, 1–19.

Meissner, J. 1969 Rheometer for the investigation of mechanical properties of plastic melts under defined extensional stress conditions. *Rheol. Acta* **8**, 78–88 (in German).

Mighri, F., Ajji, A. & Carreau, P. J. 1997 Influence of elastic properties on drop deformation in elongational flow. *J. Rheol.* **41**, 1183–1201.

Olagunju, D. O. 1999 A 1-D theory for extensional deformation of a viscoelastic filament under exponential stretching. *J. Non-Newtonian Fluid Mech.* **87**, 27–46.

Plateau, J. 1863 Experimental and theoretical researches on the figures of equilibrium of a liquid mass withdrawn from the action of gravity, etc. Annual Report of the Board of Regents of the Smithsonian Institution, Pt 1 House of Representatives Misc. Doc. 83, 38th Congress, 1st Session, pp. 207–285.

Rayleigh, Lord 1878 On the instability of jets. *Proc. Lond. Math. Soc.* **4**, 10.

Spiegelberg, S. H., Ables, D. C. & McKinley, G. H. 1996 The role of end-effects on measurements of extensional viscosity in filament stretching rheometers. *J. Non-Newtonian Fluid Mech.* **64**, 229–267.

Sridhar, T., Tirtaatmadja, V., Nguyen, D. A. & Gupta, R. K. 1991 Measurement of extensional viscosity of polymer solutions. *J. Non–Newtonian Fluid Mech.* **40**, 271–280.

Stone, H. A. 1994 Dynamics of drop deformation and breakup in viscous fluids. *Annu. Rev. Fluid Mech.* **26**, 65–102.

Tenhaeff, M. 1997 Computation of incompressible, axisymmetric flows in electrically conducting fluids under influence of rotating magnetic fields. Master thesis, Albert–Ludwigs–Universität, Freiburg i. Br (in German).

Tirtaatmadja, V. & Sridhar, T. 1993 A filament stretching device for measurement of extensional viscosity. *J. Rheol.* **37**, 1081–1102.

Yao, M. & McKinley, G. H. 1998 Numerical simulation of extensional deformations of viscoelastic liquid bridges in filament stretching devices. *J. Non–Newtonian Fluid Mech.* **74**, 47–88.

Yao, M., Spiegelberg, S. H. & McKinley, G. H. 2000 Dynamics of weakly strain-hardening fluids in filament stretching devices. *J. Non–Newtonian Fluid Mech.* **89**, 1–43.

Yildirim & Basaran, O. A. 2001 Deformation and breakup of stretching bridges of Newtonian and shear-thinning liquids: comparison of one- and two-dimensional models. *Chem. Engng Sci.* **56**, 211–233.

Zhang, X., Padgett, R. S. & Basaran, O. A. 1996 Nonlinear deformation and breakup of stretching liquid bridges. *J. Fluid Mech.* **329**, 207–245.